ACS APPLIED MATERIALS & INTERFACES

Research Article

Cite This: ACS Appl. Mater. Interfaces XXXX, XXX, XXX−XXX

www.acsami.org

Effects of Stiff Film Pattern Geometry on Surface Buckling Instabilities of Elastic Bilayers

Tetsu Ouchi,[†,§] Jiawei Yang,[‡,§] Zhigang Suo,[*,‡] and Ryan C. Hayward[*,†]

[†]Department of Polymer Science and Engineering, University of Massachusetts Amherst, Amherst, Massachusetts 01003, United States

[‡]School of Engineering and Applied Sciences, Kavli Institute for Bionano Science and Technology, Harvard University, Cambridge, Massachusetts 02138, United States

Supporting Information

ABSTRACT: Buckling instabilities—such as wrinkling and creasing—of micropatterned elastic surfaces play important roles in applications, including flexible electronics and microfluidics. In many cases, the spatial dimensions associated with the imposed pattern can compete with the natural length scale of the surface instabilities (e.g., the wrinkle wavelength), leading to a rich array of surface buckling behaviors. In this paper, we consider elastic bilayers consisting of a spatially patterned stiff film supported on a continuous and planar soft substrate. Through a combination of experimental and computational analyses, we find that three surface instability modes—wrinkling, Euler buckling, and rigid rotation—are observed for the stiff material patterns, depending on the in-plane dimensions of the film compared to the natural wrinkle wavelength, while the intervening soft regions undergo a creasing instability. The interplay between these instabilities leads to a variety of surface structures as a function of the pattern geometry and applied compressive strain, in many cases yielding contact between neighboring stiff material elements because of the formation of creases in the gaps between them.

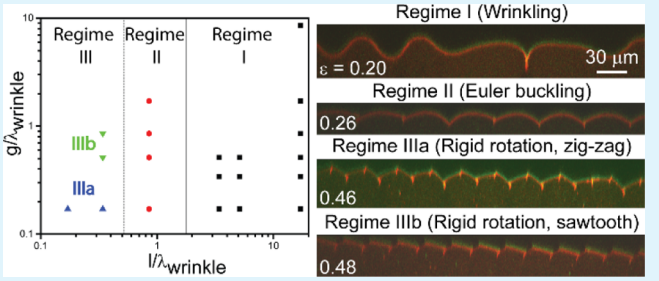

KEYWORDS: *surface instabilities, wrinkling, creasing, buckling, patterned surfaces, elastic materials*

1. INTRODUCTION

Elastic surfaces under compression can undergo a variety of buckling instabilities, such as wrinkling, creasing, cratering, folding, or ridging, depending on the elastic and geometric properties of the materials and the loading conditions.[1−3] Researchers have found numerous applications for these instabilities, including flexible electronics,[4−7] microfluidics,[8] optical devices,[9−12] tunable wetting,[13,14] adhesives,[15] measurements of thin-film mechanical properties,[16,17] and cell culture substrates.[18,19] Thanks to in-depth studies by many groups, a rather good understanding now exists of each of these surface instability modes for systems that are homogeneous in the plane.[1−3,20−26] However, many applications of these instabilities involve surfaces that are patterned into regions with different material properties (e.g., stiff conducting electrodes and soft insulating substrates in flexible electronics), and yet our fundamental understanding of surface instabilities on such heterogeneous surfaces is still lacking. Because the length scales of surface patterns in applications can often approach the natural length scales of surface instabilities (e.g., the wrinkle wavelength), a rich coupling between the imposed pattern geometry and the buckling behavior may be anticipated. In addition to possibilities for improving current applications, the broader range of complex surface topographies enabled by this coupling may open new potential for surface instabilities, such as in controlling elastic wave propagation.[27]

Recently, several studies have revealed interesting behaviors in systems with heterogeneous stiff films on soft substrates, including where the length scale of the surface pattern becomes comparable to the wrinkle wavelength.[27−35] For example, Croll et al. introduced spatial variations in film thickness through lateral phase separation of a block copolymer, yielding a coexistence of short- and long-wavelength wrinkles on a single surface.[28] Relatedly, Gurmessa et al.[32] and Wang et al.[29,30] developed bilayers with patterned thin films by controlling the exposure of silicone elastomer surfaces to UV/ozone, leading to a series of new surface topographies depending on the geometrical parameters of the imposed pattern. To date, however, there has been little work devoted to the coupling between pattern geometry and instability modes for heterogeneous surfaces consisting of a patterned stiff film surrounded by regions of a soft (elastomer or gel) substrate that may be expected to form self-contacting creases. Although two prior studies focused on patterned stiff films and bare soft substrates, the substrates were under pretension, disfavoring the formation

Received: March 26, 2018
Accepted: June 14, 2018

DOI: 10.1021/acsami.8b04916
ACS Appl. Mater. Interfaces XXXX, XXX, XXX−XXX

of creases, and thus, these papers focused primarily on the surface instabilities of the stiff patterned regions.[32,34] In one of the few examples of studies concerning the coupling between instabilities in both stiff and soft regions, our group has shown how the formation of creases in elastomeric regions between patterned stiff metal electrodes allows for the development of mechanically gated electrical switches with high on/off ratios and controlled switching strains.[7] However, the influence of pattern geometry on instability modes for either the stiff film or the soft substrate—that is, how the stiff film patterns affect the formation of creases, how creases interact with surface instability modes on the stiff patterns, and so on—has not yet been understood.

In the current study, we employ a combination of experiments and numerical simulations to characterize the instability modes of heterogeneous bilayers consisting of regularly patterned stiff film stripes supported on a soft elastomeric substrate. We monitor the evolution of surface morphology as a function of compressive strain along the direction transverse to the long axis of gaps between the stripes and find a diverse array of surface morphologies due to the combination of instabilities in the stiff and soft regions. The stiff stripes show three distinct regimes (wrinkling, Euler buckling, and rigid rotation), depending on the pattern length scale compared with the wrinkle wavelength. Moreover, the formation of creases in the soft regions greatly facilitates contact between neighboring stiff regions for certain geometries, providing a straightforward route to tune the strain for contact over a wide range.

2. METHODS

2.1. Experiment. To experimentally characterize the surface buckling of micropatterned elastic bilayers, we modified an approach that we had developed previously for homogenous bilayers (Figure 1).[36] Specifically, a polydimethylsiloxane (PDMS) (Elastosil M4600, Wacker Chemical Company) "mounting layer" was used to apply homogeneous compression to the elastic bilayer. Elastosil M4600A and Elastosil M4600B were mixed in a 10:1 ratio, followed by degassing inside of a mold defined by a glass slide and a polystyrene sheet separated by 1.2 mm thick glass spacers. After degassing, the sample was held at room temperature for 1 h to fix the shape and then cured at 75 °C for 2 h. The mounting layer was cut into rectangular pieces of ∼8 mm × 4 mm, which were uniaxially prestretched to an extension ratio of 2−3 using a stretching stage (Figure 1a). A PDMS (Sylgard 184, Dow Corning) substrate was prepared by mixing base to a cross-linker in a 40:1 ratio by weight, along with 4.5 μg of rhodamine B (Sigma-Aldrich) per 1 g of PDMS (introduced as a solution in ethanol), followed by filtration through a 5 μm filter. The mixture was degassed for 5 min until visible bubbles disappeared and then poured into the sandwich mold, which consists of a glass slide treated with (tridecafluoro-1,1,2,2-tetrahydrooctyl)-dimethylchlorosilane (Gelest) as the top layer, a Si wafer coated with a polyvinyl alcohol (PVA) (87−89% hydrolyzed, Sigma-Aldrich) sacrificial layer as the bottom layer, and 125 μm thick Kapton spacers. The molded sample was cured at 75 °C for 8 h, and then immersed in water to dissolve the PVA sacrificial layer. The PDMS substrate was washed with water and a "glue layer" of PDMS (with the same composition as the substrate) was spin-coated on it at 3500 rpm for 120 s. Next, the unstressed PDMS substrate with length L_s was attached onto the prestretched mounting layer, followed by curing at 75 °C for 8 h. After curing, the fluorinated glass slide was peeled off of the assembled PDMS substrate.

Patterned stiff films were prepared using 500 nm thick layers (measured with a Dektak 150 stylus profilometer, Veeco Instruments) of SU8 2000.5 (Micro Chem) photoresist spin-coated at 3000 rpm for 60 s onto a Ca^{2+}-cross-linked poly(acrylic acid) sacrificial layer,

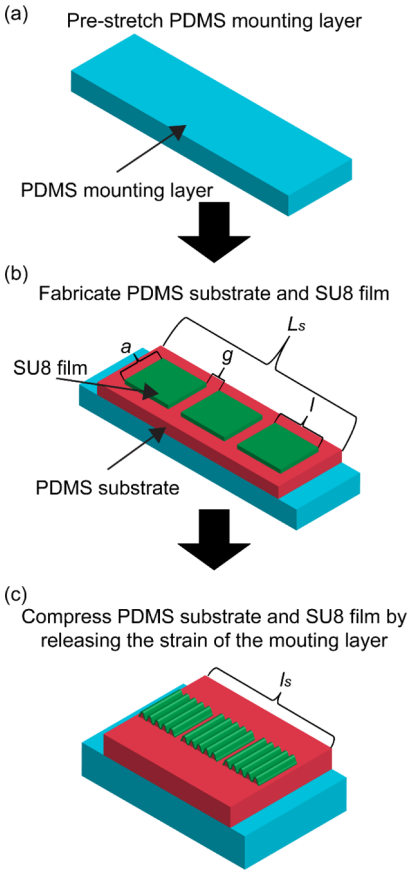

Figure 1. Schematic illustration of the experimental system: (a) the PDMS mounting layer is prestretched, (b) followed by lamination of the PDMS substrate and the patterned SU8 film, which are (c) compressed by releasing the prestrain of the mounting layer. The global strain is defined as $\varepsilon = (L_s - l_s)/L_s$.

followed by photolithographic patterning using an MA/BA 6 mask aligner (SUSS MicroTec).[37] The length of the stiff films l and gap distances g along the compression direction were varied, whereas the length perpendicular to the compression direction a was fixed as 500 μm. After photolithography, the patterned SU8 film was exposed to UV/ozone for 5 min to improve adhesion and then attached to the PDMS substrate. The assembled sample was immersed in phosphate buffered saline solution to dissolve the sacrificial layer, followed by washing with water and drying with nitrogen to complete the transfer of the patterned stiff film to the substrate (Figure 1b).

By partially releasing the prestretched mounting layer to a length l_s, a global compressive strain defined as $\varepsilon = (L_s - l_s)/L_s$ was then applied to the patterned bilayer (Figure 1c). The strain ε was measured by tracking two points on the elastomer surface located far from the patterned film regions. At high strain, delamination of the SU8 film sections occurred, starting from the edges oriented parallel to the compression direction and propagating toward the central region of the patterns. Only the central regions (farthest from where delamination initiated) were analyzed, and experiments were stopped once the delaminated area reached 25% of the patterned film area, to minimize any effects on the development of the surface morphology. Measurements of 3D surface topography were recorded using laser scanning confocal fluorescence microscopy (A1-SP; Nikon), relying on rhodamine B (red; PDMS substrate) and autofluorescence of SU8 (green; thin film) to provide fluorescence. An index-matching fluid consisting of 72 wt % of glycerol and 28 wt % of water was used with a 25× variable immersion lens. NIS Elements software was used for image analysis. When periodic patterns were observed, the tilt angle and curvature of film elements were measured within a single-ordered "grain." The tilt angle was measured from the compression direction,

DOI: 10.1021/acsami.8b04916
ACS Appl. Mater. Interfaces XXXX, XXX, XXX−XXX

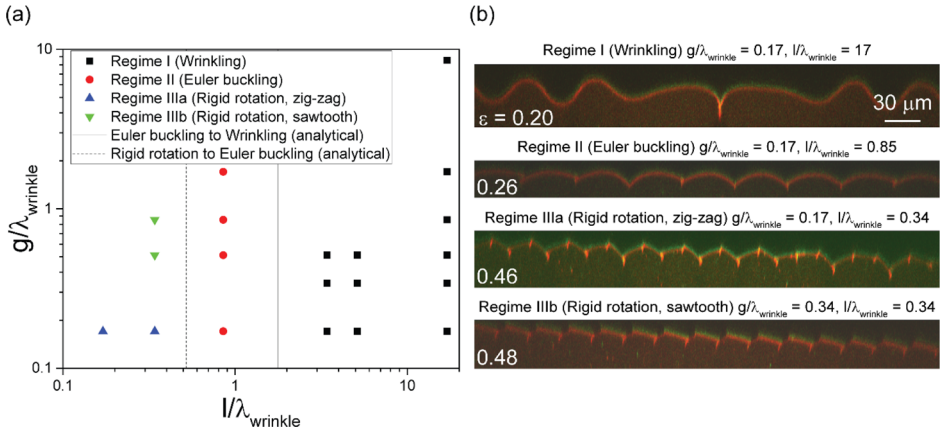

Figure 2. (a) "Phase diagram" of surface instability modes, along with (b) representative confocal fluorescence cross sections of the surface profile in each regime (red and green colors come from the PDMS substrate and the SU8 film, respectively). The values at the left bottom in each picture represent the global compressive strains. The picture in Regime I shows a region symmetric around one gap.

with positive values representing counter-clockwise rotation. The natural wrinkle wavelength $\lambda_{wrinkle,}$ was determined to be 59 μm by fitting the dependence of the measured wavelength λ on strain to the equation $\lambda = \lambda_{wrinkle}(1 - \varepsilon)$ (Figure S1) for a sample with a long rectangular pattern of SU8 (l = 8 mm, a = 500 μm). The strain for the contact of neighboring film regions was defined as the average between the largest strain where there clearly was no contact, and the smallest strain where there clearly was contact, as judged from confocal micrographs.

2.2. Simulation. The commercial finite element (FEM) software ABAQUS/standard 6.12 was used to simulate surface instabilities of patterned bilayers. Because of the difficulty of simulating the evolution of creases over large ranges of strain, direct numerical simulation of the experimental geometry was not possible. Instead, to approximate the behavior of samples with small g, we neglected the gap between the film islands and modeled each discrete film region as a beam connected to its neighbors by a freely rotating hinge (Figure S2). This approach greatly simplifies the simulations by eliminating the deformation of the substrate between the gaps. Strictly speaking, this treatment is a valid representation of the experiments only in the limit that the ratio $g/(g + l)$ approaches zero. However, we expect good qualitative agreement so long as $g/(g + l) \ll 1$, although with quantitative differences in the values of strain at which behaviors are observed in simulations and experiments.

Because of the periodic structure of the patterned film, it was sufficient to model a single film region of length l as a unit computational cell. The plane strain condition was used in the simulations. The film was modeled as an elastic beam and the substrate as an incompressible neo-Hookean material. The elastic modulus ratio and the thickness ratio of the film to the substrate were $\bar{E}_f/\bar{E}_s$ = 250 000 and H_f/H_s = 0.005. The Poisson's ratio of the film was 0.22. We employed the same thickness of the film (0.5 μm) that was used in the experiments, and the wavelength was estimated as $\lambda_{wrinkle} = 2\pi H_f(\bar{E}_f/\bar{E}_s)^{1/3}$ = 126 μm. To reproduce the different surface morphologies by the different film length, we set the film length l as 1200 μm ($l/\lambda_{wrinkle}$ = 9.5), 120 μm ($l/\lambda_{wrinkle}$ = 0.95), and 50 μm ($l/\lambda_{wrinkle}$ = 0.40). The beam was geometrically tied to the substrate to impose continuity of deformation at the interface. When the film length is larger than (l = 1200 μm) or similar to (l = 120 μm) the natural wrinkle wavelength, the film length does not affect the wrinkle wavelength. However, when the film length is smaller than (l = 50 μm) the natural wrinkle wavelength, the wavelength of buckling is specified by the film length. To break the translational symmetry beyond the onset of wrinkles, an initial geometric imperfection was introduced. It has the form of two components: The first was a stress-free surface undulation with the shape and natural wavelength of the wrinkle mode, with a very small amplitude (equal to 0.001 times the entire model thickness), whereas the second was a stress-free linear distributed vertical surface displacement with amplitude equal to 0.0001 times the entire model thickness at one end and vanishing at the other end. The first component is to trigger wrinkles and the second component is to trigger the secondary bifurcations such as period-doubling. It is noted that the second component is not the only way to trigger the period-doubling; many other methods such as using random force perturbation and pseudo-dynamic algorithm[38] are also applicable. The method to generate geometric imperfection is as follows: We prescribed the symmetric boundary condition at the left, right, and bottom sides of the computational unit cell and the displacement with the profile of the geometric imperfection to the top free surface. The displacements of all nodes were subsequently exported to a file by adding the command "*node file, global = yes u" in the keywords of the model. Next, to introduce the generated geometric imperfection for post-wrinkling analysis, we imported this file to a new model with an identical computational unit cell by using the command "*imperfection" in the keywords of the model. In the new model, on the right boundary of the unit cell, the node at the top surface of the substrate and the node at the right boundary of the beam were free to rotate but were constrained in the horizontal direction, which functioned as a hinge; the rest of the right boundary was symmetric. On the left boundary, horizontal displacement was applied to both the substrate and the film. On the bottom boundary, the horizontal displacement was free, and the vertical displacement was zero. Two analytical rigid bars were placed at the left and right boundaries of the unit cell to enable contact with the beam. The rigid bar at the right boundary was entirely fixed, whereas the rigid bar at the left boundary was subject to a horizontal displacement matching the displacement to the unit cell to simulate the contact between wrinkles. All other degrees of freedom were fixed.

3. RESULTS AND DISCUSSION

3.1. Phase Diagram of Surface Instabilities. We first briefly summarize the influence of the pattern length (l) and the gap distance (g) on surface instability modes of the stiff film in terms of a "phase diagram" based on the two dimensionless parameters $l/\lambda_{wrinkle}$ and $g/\lambda_{wrinkle}$ in Figure 2a. We find three instability regimes and four distinct surface instability patterns depending on the two dimensionless numbers. Corresponding confocal fluorescence micrographs in Figure 2b show examples of each type of behavior, with the stiff SU8 film in green and the soft PDMS substrate in red.

The instability mode is controlled by the value of $l/\lambda_{wrinkle}$. In Regime I, where $l/\lambda_{wrinkle} \gtrsim 2$ (black squares in Figure 2a), the stiff region undergoes wrinkling as the first instability mode. In Regime II, where $l/\lambda_{wrinkle} \approx 1$ (red circles), the stiff films are insufficiently wide to form multiple wrinkles, and instead undergo Euler buckling, that is, with each film segment

DOI: 10.1021/acsami.8b04916
ACS Appl. Mater. Interfaces XXXX, XXX, XXX−XXX

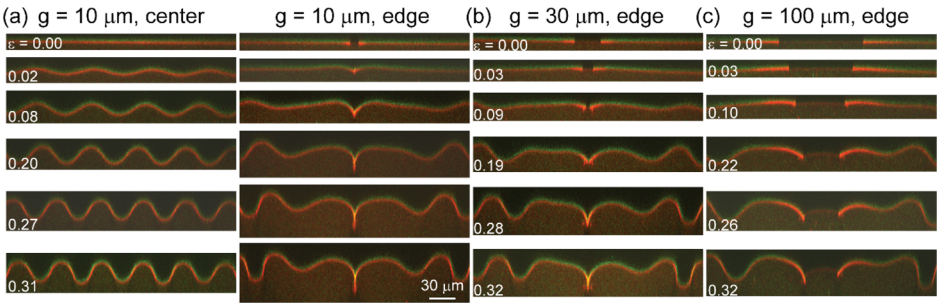

Figure 3. Surface morphology as a function of strain in Regime I (wrinkle) (l = 1000 μm, $l/\lambda_{wrinkle}$ = 17, a = 500 μm): (a) g = 10 μm, $g/\lambda_{wrinkle}$ = 0.17, (b) g = 30 μm, $g/\lambda_{wrinkle}$ = 0.51, and (c) g = 100 μm, $g/\lambda_{wrinkle}$ = 1.7. The values at the left bottom in each picture represent the global compressive strains.

adopting a single arch-like configuration. Finally, in Regime III, where $l/\lambda_{wrinkle} \lesssim 0.5$ (blue and green triangles), each film remains nearly planar but instead undergoes rigid rotation to relieve stress. Interestingly, this regime exhibits two different patterns depending on $g/\lambda_{wrinkle}$. For $g/\lambda_{wrinkle} < 0.2$, the films adopt a symmetrical "zig-zag" pattern, in which the segments alternate in a tilting direction. For $g/\lambda_{wrinkle} > 0.2$, they form an asymmetrical "sawtooth" pattern, where each segment in a single "grain" of the structure rotates in the same direction. These observed transitions between the three regimes are in good agreement with the combination of theoretical analysis and numerical simulation by Wang et al., where they assumed a single bilayer slab of length l along the compression direction (Figure 2a).[29,30] They determined the stiffness of wrinkling, Euler buckling, and rigid rotation modes by finite element simulation and analytically calculated the critical values separating each mode. The critical value predicted to separate wrinkling and Euler buckling is $l/\lambda_{wrinkle}$ = 1.77 (solid line), whereas that between Euler buckling and rigid rotation is $l/\lambda_{wrinkle}$ = 0.52 (dashed line), which matches our results. This agreement, despite the absence of gaps between rigid film elements in the calculations, suggests that at least the initial buckling mode is not highly sensitive to the details of the gap geometry.

Notably, a similar progression from wrinkling, to Euler buckling, to rigid rotation with decreasing $l/\lambda_{wrinkle}$ was found by Wang et al. for bilayers patterned into stiffer and softer regions.[29,30] However, the "soft" regions in their experiments were still thin films with much higher modulus than the underlying PDMS substrate,[29,30] whereas here, the soft regions correspond to bare PDMS. This leads to an important difference, in that for the current system, self-contacting creases are formed within the soft regions, which influences the evolution of surface instabilities of the stiff film. For example, we observe a qualitatively new zig-zag behavior in Regime III and high-strain behaviors reminiscent of "period doubling" in Regime II. Moreover, for low values of $g/\lambda_{wrinkle}$, the formation of creases facilitates contact between neighboring film patterns at low applied strains. We discuss the instability behaviors found in each regime in detail in sections 3.2−3.5.

3.2. Regime I (Wrinkling). In Regime I, where $l/\lambda_{wrinkle} \gtrsim 2$, wrinkling occurs regardless of the value of $g/\lambda_{wrinkle}$ (Figures 3a and S3). Wrinkles form first in the central region of each portion of the patterned film and propagate progressively toward the edges with an increase in strain. As the film length becomes shorter, the onset of wrinkles is progressively delayed to higher strains because of the traction-free boundary condition at the film edges, which locally reduce the strain applied to the film in the vicinity of the edge. These behaviors agree well with the results by Han et al.[39] Further compression gives rise to period-doubling (Figure S4), similar to the behavior of a homogeneous bilayer of a stiff film on a soft substrate.[23]

Interestingly, the behavior of the film edges and the bare substrate in the gap regions depends on $g/\lambda_{wrinkle}$. At low $g/\lambda_{wrinkle}$ (<1.7), shallow creases form at the edges of the stiff patterns (Figures 3a,b and S5) at very low global strain, which is consistent with the singular nature of the strain state expected at the boundary between the film and the substrate.[40] Presumably, this strain concentration allows the critical strain for creasing to be locally exceeded, even at arbitrarily small global strains, thus nucleating creases near each edge—this phenomenon will be discussed in more depth in a later paper. At larger ε, however, a large crease is formed in the center of the gap, leading to contact between neighboring film regions (Figure 3a,b). Notably, the strain for the stiff film contact is ε = 0.02 for g = 10 μm and 0.15 for g = 30 μm, which are both far below the value of 0.438 for the formation of a crease on a homogeneous elastomer surface.[22] Considering the applications of such patterned bilayers, the control of contact between patterned stiff elements is very important. For example, in flexible electronics, unintended contact can lead to short circuiting or electrical cross-talk between neighboring devices, whereas designed contact can provide strain-gated switches with very high on/off ratios.[7] This pattern contact behavior is discussed in greater detail in section 3.5.

For large $g/\lambda_{wrinkle}$ (>1.7), a different behavior is observed (Figure 3c). Creases first appear at both edges of the stiff patterns at small strains, as before. However, these two edge creases continue to grow in depth with increasing compressive strain, leading to partial "subduction" of each film edge into a crease, without the formation of a large crease in the center of the gap or contact of neighboring film regions. At even larger strains of 0.26−0.32, the crease on one side of the gap begins to grow more in depth than the other.

Finite element simulations (Figure 4) match very well with experimental observations in the small gap limit. Wrinkling occurs as the first surface instability mode of the stiff films at a very small strain. The wrinkles are uniform in the center of the film but decay in amplitude near the two edges because of the ability of the edges to freely rotate. With further compression, the wrinkles grow in amplitude, whereas the edges of the two films rotate toward each other and start to form a region of contact of non-zero length (i.e., in contrast to the initial single point of contact at the joint between the film regions) at a strain of 0.09. At ε = 0.225, the wrinkles bifurcate to a period-

DOI: 10.1021/acsami.8b04916
ACS Appl. Mater. Interfaces XXXX, XXX, XXX−XXX

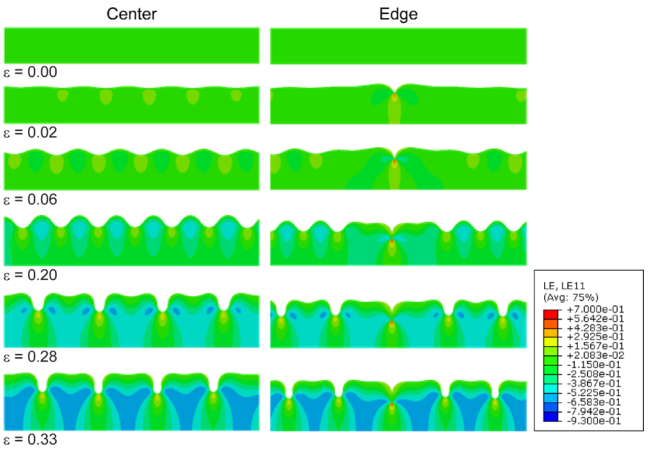

Figure 4. Simulation results in Regime I. The legend shows the local strain in the substrate along the horizontal direction.

doubled morphology, with one trough amplitude increasing at the expense of its two neighbors.

3.3. Regime II (Euler Buckling). In Regime II, where $l/\lambda_{wrinkle} \approx 1$, Euler buckling is the first instability mode for the stiff films (Figure 5). At a critical strain, each panel buckles into

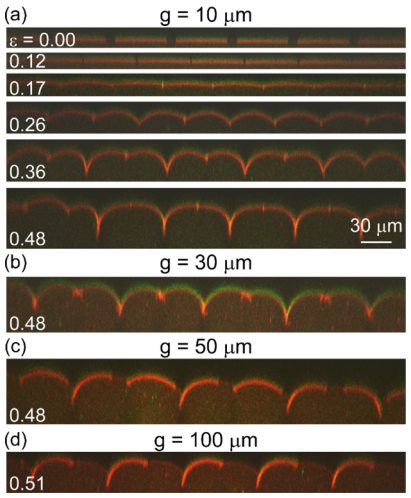

Figure 5. Surface morphology as a function of strain in Regime II (Euler buckling) (l = 50 μm, $l/\lambda_{wrinkle}$ = 0.85, a = 500 μm): (a) g = 10 μm, $g/\lambda_{wrinkle}$ = 0.17, (b) g = 30 μm, $g/\lambda_{wrinkle}$ = 0.51, (c) g = 50 μm, $g/\lambda_{wrinkle}$ = 0.85, and (d) g = 100 μm, $g/\lambda_{wrinkle}$ = 1.7. The values at the bottom left in each picture represent the global compressive strains.

a single upward arch, which progressively increases in curvature with further strain (Figure S6). As in Regime I, creases also form at small strains next to the edges of the stiff patterns because of the high stress concentration in the substrate regions adjacent to the film edges and become deeper with increased strain. Interestingly, as the compressive strain is further increased, the stiff patterns start to rotate and are partially drawn into the creases. However, the details of how the morphologies evolve at high strain depend on the value of $g/\lambda_{wrinkle}$, as we describe in the following paragraph.

For the smallest gaps (e.g., $g/\lambda_{wrinkle}$ = 0.17), each stiff film forms contact with both of its neighbors, buckles, and then undergoes a "period-doubling" in which every second crease becomes deeper, whereas the intervening creases become shallower, as seen in Figure 5a,b. This period-doubled structure is mirror symmetric and shows a clear bifurcation in the rotational angles, where neighboring plates start to rotate in opposite directions (Figure S6a,b). As $g/\lambda_{wrinkle}$ increases, this period doubling leads to asymmetric periodic structures (Figure 5c,d). For $g/\lambda_{wrinkle}$ = 0.85, the stiff plates never come into contact, and at high strains, every second film element is pulled into a deep crease, whereas the intervening plates buckle but do not rotate substantially (Figures 5c and S6c). A further increase in $g/\lambda_{wrinkle}$ = 1.7 causes each plate to rotate in the same direction at high strains (Figures 5d and S6d), yielding a "Janus"-like surface structure, which keeps the periodic unit as the initial Euler buckling morphology, that is, one stiff pattern and one gap. Although further study is required to understand this period-doubling behavior in more detail, we note that it may occur because of nonlinearity in the elastic response of the substrate limiting the amplitude of upward deflections, similar to the wrinkle to period-doubling transition seen for homogeneous bilayers.[23] Alternatively, because the thickness of the substrate layer is modest compared to the pattern length scale, we cannot rule out the possibility that the substrate thickness plays a role in selecting the wavelength of the secondary bifurcation.

Once again, FEM simulations (Figure 6) show good agreement with the experimental results in the small gap

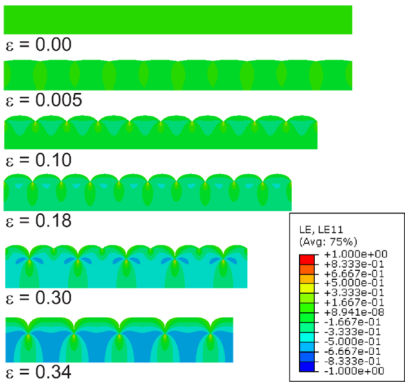

Figure 6. Simulation results in Regime II. The legend shows the local strain in the substrate along the horizontal direction.

limit. The stiff regions undergo Euler buckling, forming a symmetric and periodic pattern, with increasing curvature as strain increases. At ε = 0.21, the neighboring films start to form a line of contact of non-zero length around each hinge point. At ε = 0.30, the buckled films start to rotate, bifurcating into a period-doubled state with every second region of contact increasing in length at the expense of the intervening amplitudes. By ε = 0.34, the shallower troughs completely disappear. Although each transition happens at a slightly smaller strain (because of the zero length gap), the evolution of the surface morphology otherwise matches the experimental observations for the smallest g (Figure 5a) very closely.

3.4. Regime III (Rigid Rotation). In Regime III, where $l/\lambda_{wrinkle} \lesssim 0.5$, the length of the film elements is insufficient to allow for bending, instead leading to rigid rotation of the stiff patterns in response to the applied strain. However, two different patterns of rigid rotation are observed depending on $g/\lambda_{wrinkle}$ (Figure 7).

For the smallest gap size studied, $g/\lambda_{wrinkle}$ = 0.17 (Figure 7a), creases form at the edge of each plate, with further compression eventually leading to contact between neighbor-

DOI: 10.1021/acsami.8b04916
ACS Appl. Mater. Interfaces XXXX, XXX, XXX−XXX

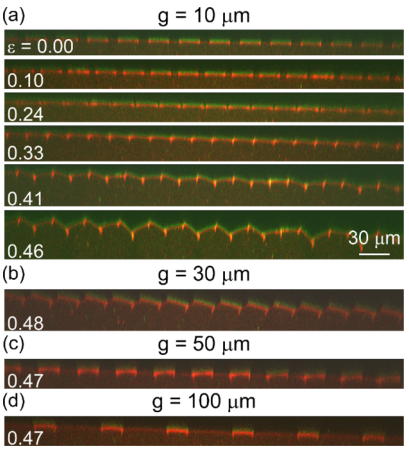

Figure 7. Surface morphology as a function of strain in Regime III (rigid rotation) (l = 20 μm, $l/\lambda_{wrinkle}$ = 0.34, a = 500 μm): (a) g = 10 μm, $g/\lambda_{wrinkle}$ = 0.17, (b) g = 30 μm, $g/\lambda_{wrinkle}$ = 0.51, (c) g = 50 μm, $g/\lambda_{wrinkle}$ = 0.85, and (d) g = 100 μm, $g/\lambda_{wrinkle}$ = 1.7. The values at the bottom left in each picture represent the global compressive strains.

ing elements, with the plates remaining almost planar and horizontal, much like in Regime II. However, additional compression leads to a bifurcation in the tilt angles (Figure S7a), in which neighboring plates tend to rotate in opposite directions, yielding a zig-zag structure (Regime IIIa, Figure S7a). Although the zig-zag morphology is fairly well-ordered and shows clear bifurcation of the tilt angles, for l = 20 μm (Figures 7a and S7a), a reduction to l = 10 μm leads to a more disordered morphology with the scattered tilt angles between 35° and −35°, in which only some regions of clear alternation are observed (Figures S8 and S7e). Although the strain to form the zig-zag structure in the simulation is smaller than in the experiments because of the zero-length gap in the former case, FEM results otherwise capture this zig-zag structure well (Figure 8). The films do not buckle but simply rotate relative to each other at very small strain, (ε < 0.01) and continue to rotate to a larger degree with increasing compression. The neighboring films eventually start to form contact over some finite length in the "troughs" of the pattern because of bending of the plates at ε = 0.44 strain. In the experiments, such bending was not observed, presumably because the strain applied subsequent to rigid rotation was not sufficiently large. In the simulations, bending is observed at a strain of 0.20 beyond that required for rigid rotation; because rigid rotation does not occur in the experiments until $\varepsilon \approx 0.40$ strain, we expect that values of $\varepsilon \approx 0.60$ would likely be required to cause bending.

For larger values of $g/\lambda_{wrinkle}$ (≥0.51), we instead find that prior to contact of the horizontal plates, each portion of the stiff film rotates in the same direction, causing the crease on the "downhill" side of the film to deepen, whereas the crease on the opposite side does not (e.g., Figure 7b), leading to a sawtooth morphology. Wang et al.[29,30] found a similar sawtooth structure through both simulation and experiment for samples patterned into stiffer and softer bilayer regions when $l/\lambda_{wrinkle}$ < 0.52. However, in their system, the softer bilayer region (still capped with a film that is much stiffer than the substrate) undergoes Euler buckling, whereas in the current case, the formation of creases in the intervening soft substrate enables the sawtooth structure. As the formation of periodic patterns relies on the interaction between the stiff regions, increasing $g/\lambda_{wrinkle}$ leads to less regular patterns and smaller tilting angles (Figure 7b–d). For example, the stiff patterns with $g/\lambda_{wrinkle}$ = 0.51 show tilting angles with a magnitude of approximately 17° at 0.48 strain (Figure S7b), whereas those with $g/\lambda_{wrinkle}$ = 0.85 show tilting angles with a magnitude of approximately 5° at 0.47 strain (Figure S7c).

3.5. Contact of the Stiff Patterns Induced by Surface Instabilities. The ability of neighboring stiff regions to form contact because of surface instabilities is one of the most interesting, and potentially attractive, features of such patterned bilayer films. Controlling this contact, and the strain at which it occurs, may not only provide a means to prevent short circuits in flexible electronics but also has the potential for applications, such as flexible electronic switches, or surfaces with highly tunable wettability. In this section, the contacting behavior in each regime is discussed and compared with the prediction of a simple model, as summarized in Figure 9.

The presence or absence of contact between film regions and the strain necessary to achieve it strongly depend on the instability modes. First, in Regime I, where $l/\lambda_{wrinkle}$ = 3 to 17 (circle, triangle, and square points in Figure 9), contact occurs when $g/\lambda_{wrinkle}$ is small enough for the creases at the edge of each plate to combine into a single centered crease: $g/\lambda_{wrinkle}$ =

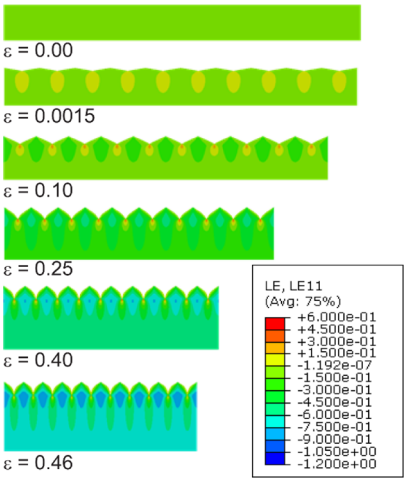

Figure 8. Simulation results in Regime III. The legend shows the local strain in the substrate along the horizontal direction.

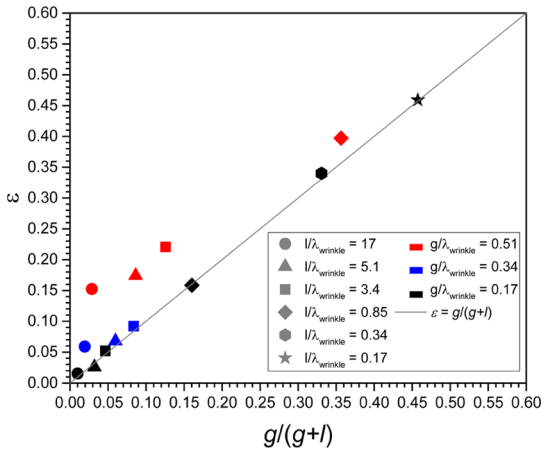

Figure 9. Strain for contact plotted against the fraction of surface length represented by the gaps in the undeformed state.

DOI: 10.1021/acsami.8b04916
ACS Appl. Mater. Interfaces XXXX, XXX, XXX−XXX

0.17 to 0.51 in Figures 3 and S3. When $g/\lambda_{wrinkle}$ is too large, the creases at the plate edges both become deeper, preventing contact (Figure 3c). Interestingly, this regime allows the strain for contact to be tuned from very small values (e.g., $\varepsilon = 0.02$ for $l/\lambda_{wrinkle} = 17$ and $g/\lambda_{wrinkle} = 0.17$) up to substantially larger strains (e.g., $\varepsilon = 0.22$ for $l/\lambda_{wrinkle} = 3.4$ and $g/\lambda_{wrinkle}$ 0.51). In Regime II, where $l/\lambda_{wrinkle} = 0.85$ (diamond points), if $g/\lambda_{wrinkle}$ is short enough, contact occurs on both sides of each plate before rotation starts ($g/\lambda_{wrinkle} = 0.17$ and 0.51 in Figures 5a,b and S6a,b). However, if $g/\lambda_{wrinkle}$ is larger, rotation occurs first, thereby preventing contact over the range of strains studied (e.g., $g/\lambda_{wrinkle} = 1.7$ in Figure 5d). Finally, in Regime III, where $l/\lambda_{wrinkle} = 0.17$ and 0.34 (hexagon and star points), contact occurs only for the zig-zag structures formed at small gap sizes and requires large compression $\varepsilon > 0.30$. For larger gaps, the asymmetrical nature of the sawtooth structure prevents contact between stiff patterns.

In the limiting case that the plates do not buckle, we can idealize the stiff material regions as fixed at their initial length l, such that all of the globally applied strain is absorbed by the deformation of the soft material in the gaps. This leads to the simple prediction for the strain at a contact of $g/(g + l)$, shown as a solid line in Figure 9. Intriguingly, this simple prediction matches the experimental results very well for $g/\lambda_{wrinkle} = 0.17$ (black points in Figure 9) in all three regimes, and for $g/\lambda_{wrinkle} = 0.34$ (blue points) other than at the largest value of $l/\lambda_{wrinkle}$. For the largest value of $g/\lambda_{wrinkle} = 0.51$ (red points), where contact was observed, the contact strains lie significantly above the prediction, especially in the wrinkling and Euler buckling regimes because the rigid elements have buckled to substantial amplitude prior to contact. In any case, Figure 9 provides a simple guide for how the critical strain for pattern contact can be tuned over a wide range (from $\varepsilon = 0.02$ to 0.46) by the appropriate choice of pattern geometry.

4. CONCLUSIONS

The effects of pattern geometry on surface instability modes of bilayers with discontinuous stiff material stripes on a soft elastomeric substrate were analyzed, revealing a rich set of surface morphologies originating from the combination of different instabilities in the stiff and soft regions. In Regime I ($l/\lambda_{wrinkle} \gtrsim 2$), the films undergo wrinkling and subsequent period-doubling with increasing compression. In Regime II ($l/\lambda_{wrinkle} \approx 1$), the stiff patterns are not sufficiently long to accommodate wrinkles and thus undergo Euler buckling instead, whereas in Regime III ($l/\lambda_{wrinkle} \lesssim 0.5$), they do not buckle but instead undergo rigid rotation. Interestingly, this last regime has two types of surface instability patterns, depending on the gap size: For small $g/\lambda_{wrinkle}$, symmetric zig-zag patterns occur, whereas for large $g/\lambda_{wrinkle}$, asymmetric sawtooth patterns appear. Not only do these transitions show good agreement with previous analytical results for a single bilayer slab,[29,30] but simulations performed here also showed excellent agreement with the experiments for the small-gap cases in all three regimes.

Notably, the presence of the bare soft substrate in the gaps allows for the formation of self-contacting creases, which significantly affects the development of the surface topographies with increasing compression and also induces contact between neighboring stiff material patterns. The presence or absence of the contact, and the critical strain for contact, can be controlled by both $g/\lambda_{wrinkle}$ and $l/\lambda_{wrinkle}$ over a very wide range of strain (e.g., from 0.02 to 0.46 for patterns studied here). For sufficiently small gap sizes, the strain for contact can be understood simply by treating the stiff patterns as undeformable during compression. We expect that the fundamental understanding developed here can be applied to a wide variety of material systems (e.g., conducting or hydrophilic stiff films), enabling advances in areas such as flexible electronics, microfluidics, and surfaces with tunable adhesion and surface wettability.

■ ASSOCIATED CONTENT

Supporting Information

The Supporting Information is available free of charge on the ACS Publications website at DOI: 10.1021/acsami.8b04916.

Natural wavelength of wrinkles; simulation model; typical initial surface instabilities with different pattern lengths in Regime I; period-doubling structure; the magnified view around the gap area; tilting angle and curvature of the stiff patterns in Regime II; tilting angle of the stiff patterns in Regime III; and zig-zag structure with $g = 10\ \mu m$ (PDF)

■ AUTHOR INFORMATION

Corresponding Authors

*E-mail: suo@seas.harvard.edu (Z.S.).
*E-mail: hayward@umass.edu (R.C.H.).

ORCID

Zhigang Suo: 0000-0002-4068-4844
Ryan C. Hayward: 0000-0001-6483-2234

Author Contributions

§T.O. and J.Y. contributed equally to this work.

Notes

The authors declare no competing financial interest.

■ ACKNOWLEDGMENTS

The work at UMass was supported by the Defense Threat Reduction Agency through grant HDTRA-1-15-1-0030, whereas that at Harvard was supported by MRSEC (DMR-14-20570). The authors thank Dr. James Chambers for useful discussion and assistance with confocal microscopy experiments. The confocal microscopy data were gathered in the Light Microscopy Facility and Nikon Center of Excellence at the Institute for Applied Life Sciences, UMass Amherst, with support from the Massachusetts Life Sciences Center. The authors also thank John Nicholson and the Nanofabrication Cleanroom Facility at the Institute for Applied Life Sciences, UMass Amherst, for useful discussion and assistance with sample fabrication.

■ REFERENCES

(1) Chen, D.; Yoon, J.; Chandra, D.; Crosby, A. J.; Hayward, R. C. Stimuli-Responsive Buckling Mechanics of Polymer Films. *J. Polym. Sci., Part B: Polym. Phys.* **2014**, *52*, 1441−1461.

(2) Rodríguez-Hernández, J. Wrinkled Interfaces: Taking Advantage of Surface Instabilities to Pattern Polymer Surfaces. *Prog. Polym. Sci.* **2015**, *42*, 1−41.

(3) Genzer, J.; Groenewold, J. Soft Matter with Hard Skin: From Skin Wrinkles to Templating and Material Characterization. *Soft Matter* **2006**, *2*, 310−323.

(4) Kim, D.-H.; Ahn, J.-H.; Choi, W. M.; Kim, H.-S.; Kim, T.-H.; Song, J.; Huang, Y. Y.; Liu, Z.; Lu, C.; Rogers, J. A. Stretchable and Foldable Silicon Integrated Circuits. *Science* **2008**, *320*, 507−511.

DOI: 10.1021/acsami.8b04916
ACS Appl. Mater. Interfaces XXXX, XXX, XXX−XXX

(5) Su, Y.; Ping, X.; Yu, K. J.; Lee, J. W.; Fan, J. A.; Wang, B.; Li, M.; Li, R.; Harburg, D. V.; Huang, Y.; Yu, C.; Mao, S.; Shim, J.; Yang, Q.; Lee, P.-Y.; Armonas, A.; Choi, K.-J.; Yang, Y.; Paik, U.; Chang, T.; Dawidczyk, T. J.; Huang, Y.; Wang, S.; Rogers, J. A. In-Plane Deformation Mechanics for Highly Stretchable Electronics. *Adv. Mater.* **2017**, *29*, 1604989.
(6) Rogers, J. A.; Someya, T.; Huang, Y. Materials and Mechanics for Stretchable Electronics. *Science* **2010**, *327*, 1603−1607.
(7) Xu, B.; Chen, D.; Hayward, R. C. Mechanically Gated Electrical Switches by Creasing of Patterned Metal/Elastomer Bilayer Films. *Adv. Mater.* **2014**, *26*, 4381−4385.
(8) Khare, K.; Zhou, J.; Yang, S. Tunable Open-Channel Microfluidics on Soft Poly(Dimethylsiloxane) (PDMS) Substrates with Sinusoidal Grooves. *Langmuir* **2009**, *25*, 12794−12799.
(9) Lee, S. G.; Lee, D. Y.; Lim, H. S.; Lee, D. H.; Lee, S.; Cho, K. Switchable Transparency and Wetting of Elastomeric Smart Windows. *Adv. Mater.* **2010**, *22*, 5013−5017.
(10) Harrison, C.; Stafford, C. M.; Zhang, W.; Karim, A. Sinusoidal Phase Grating Created by a Tunably Buckled Surface. *Appl. Phys. Lett.* **2004**, *85*, 4016−4018.
(11) Görrn, P.; Lehnhardt, M.; Kowalsky, W.; Riedl, T.; Wagner, S. Elastically Tunable Self-Organized Organic Lasers. *Adv. Mater.* **2011**, *23*, 869−872.
(12) Chan, E. P.; Crosby, A. J. Fabricating Microlens Arrays by Surface Wrinkling. *Adv. Mater.* **2006**, *18*, 3238−3242.
(13) Ohzono, T.; Monobe, H. Morphological Transformation of a Liquid Micropattern on Dynamically Tunable Microwrinkles. *Langmuir* **2010**, *26*, 6127−6132.
(14) Chung, J. Y.; Youngblood, J. P.; Stafford, C. M. Anisotropic Wetting on Tunable Micro-Wrinkled Surfaces. *Soft Matter* **2007**, *3*, 1163−1169.
(15) Chan, E. P.; Karp, J. M.; Langer, R. S. A "Self-Pinning" Adhesive Based on Responsive Surface Wrinkles. *J. Polym. Sci., Part B: Polym. Phys.* **2011**, *49*, 40−44.
(16) Stafford, C. M.; Harrison, C.; Beers, K. L.; Karim, A.; Amis, E. J.; VanLandingham, M. R.; Kim, H.-C.; Volksen, W.; Miller, R. D.; Simonyi, E. E. A Buckling-Based Metrology for Measuring the Elastic Moduli of Polymeric Thin Films. *Nat. Mater.* **2004**, *3*, 545−550.
(17) Reyes-Martinez, M. A.; Ramasubramaniam, A.; Briseno, A. L.; Crosby, A. J. The Intrinsic Mechanical Properties of Rubrene Single Crystals. *Adv. Mater.* **2012**, *24*, 5548−5552.
(18) Chen, D.; Hyldahl, R. D.; Hayward, R. C. Creased Hydrogels as Active Platforms for Mechanical Deformation of Cultured Cells. *Lab Chip* **2015**, *15*, 1160−1167.
(19) Kim, J.; Yoon, J.; Hayward, R. C. Dynamic Display of Biomolecular Patterns through an Elastic Creasing Instability of Stimuli-Responsive Hydrogels. *Nat. Mater.* **2010**, *9*, 159−164.
(20) Hong, W.; Zhao, X.; Suo, Z. Formation of Creases on the Surfaces of Elastomers and Gels. *Appl. Phys. Lett.* **2009**, *95*, 111901.
(21) Hohlfeld, E.; Mahadevan, L. Unfolding the Sulcus. *Phys. Rev. Lett.* **2011**, *106*, 105702.
(22) Chen, D.; Cai, S.; Suo, Z.; Hayward, R. C. Surface Energy as a Barrier to Creasing of Elastomer Films: An Elastic Analogy to Classical Nucleation. *Phys. Rev. Lett.* **2012**, *109*, 038001.
(23) Brau, F.; Vandeparre, H.; Sabbah, A.; Poulard, C.; Boudaoud, A.; Damman, P. Multiple-Length-Scale Elastic Instability Mimics Parametric Resonance of Nonlinear Oscillators. *Nat. Phys.* **2011**, *7*, 56−60.
(24) Wang, Q.; Zhang, L.; Zhao, X. Creasing to Cratering Instability in Polymers under Ultrahigh Electric Fields. *Phys. Rev. Lett.* **2011**, *106*, 118301.
(25) Cao, Y.; Hutchinson, J. W. Wrinkling Phenomena in Neo-Hookean Film/Substrate Bilayers. *J. Appl. Mech.* **2012**, *79*, 031019.
(26) Zang, J.; Zhao, X.; Cao, Y.; Hutchinson, J. W. Localized Ridge Wrinkling of Stiff Films on Compliant Substrates. *J. Mech. Phys. Solids* **2012**, *60*, 1265−1279.
(27) Li, G.-Y.; Zheng, Y.; Cao, Y.; Feng, X.-Q.; Zhang, W. Controlling Elastic Wave Propagation in a Soft Bilayer System via Wrinkling-Induced Stress Patterns. *Soft Matter* **2016**, *12*, 4204−4213.
(28) Croll, A. B.; Crosby, A. J. Pattern Driven Stress Localization in Thin Diblock Copolymer Films. *Macromolecules* **2012**, *45*, 4001−4006.
(29) Wang, J.; Li, B.; Cao, Y.-P.; Feng, X.-Q.; Gao, H. Wrinkling Micropatterns Regulated by a Hard Skin Layer with a Periodic Stiffness Distribution on a Soft Material. *Appl. Phys. Lett.* **2016**, *108*, 021903.
(30) Wang, J.-W.; Li, B.; Cao, Y.-P.; Feng, X.-Q. Surface Wrinkling Patterns of Film-Substrate Systems With a Structured Interface. *J. Appl. Mech.* **2015**, *82*, 051009.
(31) Yan, D.; Zhang, K.; Hu, G. Wrinkling of Structured Thin Films via Contrasted Materials. *Soft Matter* **2016**, *12*, 3937−3942.
(32) Gurmessa, B. J.; Croll, A. B. Localization in an Idealized Heterogeneous Elastic Sheet. *Soft Matter* **2017**, *13*, 1764−1772.
(33) Zhao, Y.; Han, X.; Li, G.; Lu, C.; Cao, Y.; Feng, X.-Q.; Gao, H. Effect of Lateral Dimension on the Surface Wrinkling of a Thin Film on Compliant Substrate Induced by Differential Growth/Swelling. *J. Mech. Phys. Solids* **2015**, *83*, 129−145.
(34) Nogales, A.; del Campo, A.; Ezquerra, T. A.; Rodríguez-Hernández, J. Wrinkling and Folding on Patched Elastic Surfaces: Modulation of the Chemistry and Pattern Size of Microwrinkled Surfaces. *ACS Appl. Mater. Interfaces* **2017**, *9*, 20188−20195.
(35) Wang, D.; Cheewaruangroj, N.; Li, Y.; McHale, G.; Jiang, Y.; Wood, D.; Biggins, J. S.; Xu, B. B. Spatially Configuring Wrinkle Pattern and Multiscale Surface Evolution with Structural Confinement. *Adv. Funct. Mater.* **2018**, *28*, 1704228.
(36) Auguste, A.; Jin, L.; Suo, Z.; Hayward, R. C. The Role of Substrate Pre-Stretch in Post-Wrinkling Bifurcations. *Soft Matter* **2014**, *10*, 6520−6529.
(37) Linder, V.; Gates, B. D.; Ryan, D.; Parviz, B. A.; Whitesides, G. M. Water-Soluble Sacrificial Layers for Surface Micromachining. *Small* **2005**, *1*, 730−736.
(38) Zhao, Y.; Cao, Y.; Hong, W.; Wadee, M. K.; Feng, X.-Q. Towards a Quantitative Understanding of Period-Doubling Wrinkling Patterns Occurring in Film/Substrate Bilayer Systems. *Proc. R. Soc. A* **2014**, *471*, 20140695.
(39) Han, X.; Zhao, Y.; Cao, Y.; Lu, C. Controlling and Prevention of Surface Wrinkling via Size-Dependent Critical Wrinkling Strain. *Soft Matter* **2015**, *11*, 4444−4452.
(40) Lu, N.; Zhang, Z.; Yoon, J.; Suo, Z. Singular Stress Fields at Corners in Flip-Chip Packages. *Eng. Fract. Mech.* **2012**, *86*, 38−47.

DOI: 10.1021/acsami.8b04916
ACS Appl. Mater. Interfaces XXXX, XXX, XXX−XXX